Frontiers in Heat and Mass Transfer

Tech Science Press

Doi:10.32604/fhmt.2025.067385

ARTICLE

Enhanced Flow Boiling Heat Transfer of HFE-7100 in Open Microchannels Using Micro-Nano Composite Structures

Liaofei Yin[1,*], Kexin Zhang[1], Tianjun Qin[1], Wenhao Ma[1], Yi Ding[1] and Yawei Xu[2,*]

[1]Beijing Key Laboratory of Flow and Heat Transfer of Phase Changing in Micro and Small Scale, School of Mechanical, Electronic and Control Engineering, Beijing Jiaotong University, Beijing, 100044, China

[2]National Key Laboratory of Spacecraft Thermal Control, Beijing Institute of Spacecraft System Engineering, Beijing, 100094, China

*Corresponding Authors: Liaofei Yin. Email: yinliaofei@bjtu.edu.cn; Yawei Xu. Email: 18792530289@163.com

Received: 01 May 2025; Accepted: 30 May 2025; Published: 30 June 2025

ABSTRACT: Flow boiling in open microchannels offers highly efficient heat transfer performance and has attracted increasing attention in the fields of heat transfer and thermal management of electronic devices in recent years. However, the continuous rise in power density of electronic components imposes more stringent requirements on the heat transfer capability of microchannel flow boiling. HFE-7100, a dielectric coolant with favorable thermophysical properties, has become a focal point of research for enhancing flow boiling performance in open microchannels. The flow boiling heat transfer performance of HFE-7100 was investigated in this study by fabricating micro-nano composite structures on the bottom surface of open microchannels using laser ablation technology. Based on visualization results, a comparative analysis was conducted on the bubble dynamics and flow pattern characteristics of HFE-7100 flow boiling in micro-nano structured open microchannels (MNSOMC) and smooth-surface open microchannels (SSOMC), to elucidate the enhancement mechanism of micro-nano structures on flow boiling heat transfer in open microchannels. The results indicate that the surface structures and strong wettability of MNSOMC accelerated bubble nucleation and departure. Moreover, bubbles in the channel tended to coalesce along the flow direction, forming elongated slug bubbles with high aspect ratios, which enabled efficient thin film evaporation in conjunction with intense nucleate boiling, thereby significantly enhancing flow boiling heat transfer. Under the experimental conditions of this study, the maximum enhancements in the heat transfer coefficient (HTC) and critical heat flux (CHF) of HFE-7100 in MNSOMC were 33.4% and 133.1%, respectively, with the CHF reaching up to 1542.3 $kW \cdot m^{-2}$. Furthermore, due to the superior wettability and capillary wicking capability of the micro-nano composite structures, the significant enhancement in flow boiling heat transfer was achieved without incurring a noticeable pressure drop penalty.

KEYWORDS: Open microchannel; laser ablation; micro-nano composite structures; flow boiling; heat transfer enhancement

1 Introduction

With advancements in packaging technologies, electronic devices are rapidly evolving toward miniaturization, posing unprecedented challenges for thermal management systems [1]. The continuous increase in heat flux adversely affects both the performance and lifespan of electronic components. Traditional cooling methods such as finned heat exchangers, air cooling, and water cooling are no longer sufficient to meet the cooling demands of modern high-performance devices. Microchannels have attracted significant attention in the field of electronics cooling due to their compact structure, small size, and the ability to efficiently remove heat through the latent heat of vaporization during boiling [2–4].

Compared with conventional closed microchannel structures, open microchannels feature an open space above the channels, which increases the density of effective nucleation sites. This configuration enhances HTC and CHF while simultaneously reducing pressure drop, thereby significantly boosting the overall heat transfer performance of microchannels [5]. A significant number of scholars have investigated the application of open structures to improve heat transfer during flow boiling in microchannels. Zhao et al. [6] investigated the bubble dynamics and flow boiling performance in open microchannels with large aspect ratios through flow visualization. Under the combined effects of wall confinement, evaporation, buoyancy, and inertial forces, nucleated bubbles were observed to elongate and rise after growth. Notably, wall confinement and buoyancy were identified as the primary mechanisms facilitating rapid bubble migration into the open space. Bhandari et al. [7] explored open microchannel heat sinks with varying channel heights and found that the configuration with a 1.5 mm channel height achieved the best heat transfer performance. However, when the channel height increased to 1.75 and 2.0 mm, the thermal dissipation ability of the channels declined. In a subsequent study, Bhandari et al. [8] compared the flow boiling characteristics of open and closed microchannels using deionized water as the working fluid. Their experimental results showed that, compared to closed microchannels, the enhanced heat transfer in open microchannels is primarily attributed to reduced flow resistance in the open space, resulting in lower overall pressure drop.

Surface modification with micro/nanostructures significantly affects the boiling heat transfer performance of working fluids [9,10]. The influence mechanism of micro/nanostructures on liquid transport and boiling heat transfer performance involves a complex interplay of numerous microscopic processes and macroscopic phenomena. Chang et al. [11] conducted flow boiling experiments of HFE-7100 in micro-ribbed channels with nanowires and demonstrated that the micro/nanostructures effectively separated the two-phase flow, alleviated the delay in nucleate boiling onset, and regulated multiple flow regimes into annular flow to enhance heat removal ability. Zhuang et al. [12] investigated flow boiling of HFE-7100 in a microchannel with micro pin fins, revealing that this novel structure had better two-phase heat transfer performance for dielectric fluorinated fluids along with much lower pressure drop penalty compared with similar works reported by other researchers. Li et al. [13] produced micro-pin-fin fences on the side wall of parallel microchannels and obtained the significant enhancements of HTC and CHF for HFE-7100, which was attributed to the sustainable thin film evaporation due to the improved capillary action of channel walls. Yang et al. [14] examined HFE-7000 flow boiling in parallel minichannels with nanowires surfaces. The HTC was greatly enhanced due to the nanowire-improved nucleate boiling and liquid film evaporation, while the pressure drop of two-phase flow was effectively reduced by the two-phase separation and capillary flow. Alam et al. [15] performed flow boiling visualization studies using HFE-7100 and found that the micro/nanostructures promoted explosive boiling, reduced bubble departure diameters, and stabilized flow pattern transitions. These structures shortened the existence region of intermittent flow and facilitated liquid rewetting, thereby improving heat transfer while reducing pressure drop. However, micro/nanostructure-modified surfaces do not always guarantee improved boiling heat transfer. Zhou et al. [16] performed pool boiling experiments using dual-layer porous metal foams with varying porosity parameters and observed that such structures hindered bubble departure, thereby deteriorating heat transfer performance. Khan et al. [17] fabricated a micro/nano composite surface by coating sintered micro-sized copper powders with CuO nanoparticles. However, compared to the single microstructured surface, the HTC and CHF decreased by 24% and 16.8%, respectively, which was attributed to vapor generation in the nanostructures disrupting the liquid–vapor flow pathways of the microstructures, thus inhibiting capillary wetting and liquid replenishment. Liu et al. [18] analyzed the impact of nanostructure location on boiling heat dissipation in micro/nano composite surfaces and demonstrated that nanostructures can regulate bubble dynamics. However, under saturated boiling conditions, violent bubble coalescence obstructed liquid

transport, leading to a reduction in CHF. Shin et al. [19] observed that when using highly wettable FC-72 as the boiling working fluid, the capillary wicking performance of nanowire surfaces was diminished, limiting heat transfer enhancement. This, combined with the influence of nucleation sites and forced convective boiling, contributed to a reduction in CHF. The above research results show that the mechanism by which micro-nanostructures affect boiling characteristics has not yet been fully understood.

Electronic fluorinated liquids possess excellent thermophysical properties, making them highly promising for various engineering applications, particularly in electronics cooling. Among them, HFE-7100 is a commonly used dielectric coolant in electronic thermal management due to its colorlessness, non-flammability, environmental compatibility, low viscosity, and low dielectric constant. Laser ablation is a simple and efficient surface modification technique capable of precisely controlling the morphology and dimensional parameters of micro/nanostructures. It significantly increases the effective heat exchange area of the surface and holds great potential for promoting efficient liquid transport and enhancing flow boiling performance.

In this study, an experimental system for investigating heat dissipation and pressure drop of HFE-7100 flow boiling in microchannels was established. Two types of open microchannels were designed and fabricated: a smooth surface open microchannel (SSOMC) and a laser-ablated micro-nano structured open microchannel (MNSOMC). Based on visualization results, the HFE-7100 subcooled flow boiling characteristics in both types of open microchannels were comparatively analyzed, and the mechanisms by which micro/nano composite structures influence flow boiling in open microchannels were investigated.

2 Experimental Methods

2.1 Experimental System

A flow boiling experimental system was developed, as illustrated in Fig. 1. The system was primarily composed of several key components: a fluid circulation system, a preheating and a condensation system, a data acquisition and a visualization system, and the test section. The complete configuration was thermally insulated to reduce heat loss. Prior to the experiment, the pump was activated to initiate the fluid circulation, and the mass flow rate of the working fluid HFE-7100 was adjusted by regulating the speed of the gear pump. A preheater was used to control the HFE-7100 inlet temperature entering the test section to 30°C. A chiller cooled the two-phase fluid exiting the test section, condensing it completely back into liquid, which then returned to the reservoir to complete the cycle. During the experiment, the heating power of the electric rods was controlled by adjusting the voltage output of a DC power source, while K-type thermocouples and pressure sensors were employed to detect the temperature and pressure at both the inlet and outlet of the test section. An Agilent data acquisition unit was employed for data collection and recording. A high-speed camera positioned above the test section captured the bubble dynamics and flow pattern transitions within the microchannels test section.

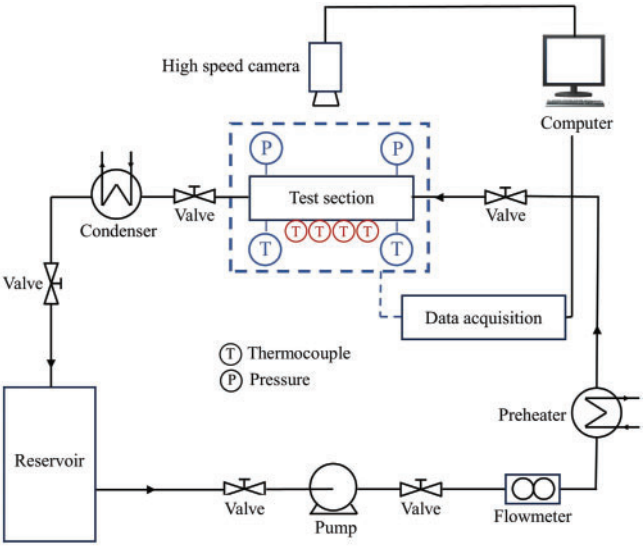

Figure 1: Experimental system of flow boiling

2.2 Test Section

In this study, two types of microchannels were designed for comparative experimental investigation: a smooth surface open microchannel (SSOMC) and a micro-nano structured open microchannel (MNSOMC) fabricated via laser ablation. A schematic of the microchannel test section is shown in Fig. 2. The microchannel comprises eight parallel channels, each with a length of 20 mm, a width of 0.4 mm, a rib width of 0.4 mm, and a height of 0.8 mm. Annular silicone gaskets was placed between the heat sink and the polysulfone cover plate to ensure sealing. A 0.5 mm gap was set between the top of the microchannel ribs and the cover plate to form an open space, thereby constructing an open microchannel structure. Twelve thermocouple holes, arranged in 3 rows and 4 columns, were drilled beneath the microchannels along the flow direction. Each hole has a diameter of 1 mm, with both transverse and longitudinal spacing of 4 mm. The top row of thermocouple holes was positioned 3.7 mm below the microchannel wall surface. Four electric heating rods were evenly embedded in the copper block to supply heat to the test section via electrical heating, each with a rated power of 500 W. The entire test section was bolted together and wrapped with thermal insulation cotton to minimize external heat loss.

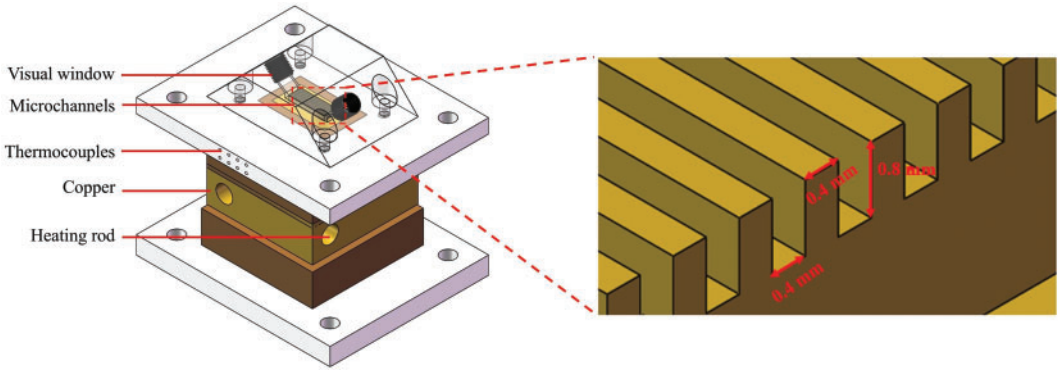

Figure 2: Schematic diagram of test section

Femtosecond laser processing is a high-precision machining technique that utilizes ultrashort laser pulses and offers advantages such as high resolution, non-contact operation, and a minimal heat-affected zone. When the laser pulse exceeds the ablation threshold, the recoil pressure generated by the phase transition of the metal causes the liquefied material to move laterally along both sides of each laser beam, forming microcavity structures [20], while also generating a large number of nanoscale depressions, protrusions, and countless tiny pores and branches. A micro-nano composite structure can be constructed on the lower surface of the SSOMC, thereby producing the MNSOMC. Inspired by natural multiscale surfaces such as honeycomb coral, which exhibit excellent liquid transport capacity and vapor venting performance, the square microgrids array with rich nanoscale features were expected to be fabricated. Femtosecond laser pulses were emitted by the laser source, and orthogonal line scanning was performed on the bottom surface of the SSOMC, which was fixed on a three-dimensional micro-displacement platform, using a laser power of 2 $J \cdot cm^{-2}$ and a scanning speed of 1 $mm \cdot s^{-1}$. The scanning intervals were controlled at 30 μm, forming a micro-nano composite structure with square microgrids, each with a depth of 40 μm and edge lengths of 30 μm. It is worth noting that this study focuses on a representative micro-nano composite structure fabricated by femtosecond laser ablation. While this approach enables fundamental insights, a broader set of structure variations is required in future studies to generalize the observed influence mechanisms.

Wettability tests were conducted on both the smooth and micro-nano composite structured surfaces. Using HFE-7100 as the working fluid, the static contact angles measured were close to 0° for both surfaces. To further investigate the wettability difference between the two heat transfer surfaces, contact angle measurements were also performed using deionized water [21]. The micro-nano composite structured surface exhibited a contact angle of 20°, compared to 78° for the smooth surface, indicating that the laser-ablated micro-nano structured surface possesses significantly enhanced hydrophilicity. In addition, to further evaluate the differences in liquid wicking behavior between the both tested surfaces, a quantitative wicking rate measurement was conducted using the method proposed by Zhang et al. [22]. Under normal temperature and pressure, the wicking rates of SSOMC and MNSOMC were determined to be 1.51×10^{-6} $m^3 \cdot s^{-1}$ and 3.20×10^{-6} $m^3 \cdot s^{-1}$, respectively. These results indicated that, for HFE-7100, the MNSOMC surface exhibited significantly enhanced wettability and capillary wicking ability compared to the smooth counterpart. Scanning electron microscope (SEM) images of the smooth surface and the micro-nano composite structured surface are shown in Fig. 3, revealing a uniformly distributed microgrid array on the modified surface, along with nanoscale stripe and particulate structures.

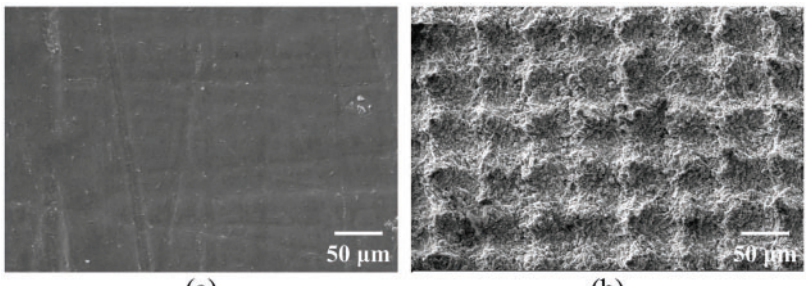

Figure 3: SEM image of surface morphology: (**a**) SSOMC; (**b**) MNSOMC

3 Data Reduction

The effective heat flux at the heat transfer surface is determined using Fourier's equation of heat conduction:

$$q = -\lambda_{\mathrm{Cu}} \frac{dT}{dx} \tag{1}$$

λ_{Cu} is the thermal conductivity of copper, taken as 391 $\mathrm{W{\cdot}m^{-1}{\cdot}K^{-1}}$.

A Taylor series expansion is used to estimate the longitudinal temperature differential beneath the heat transfer surface:

$$\frac{dT}{dx} \cong \frac{3T_1 - 4T_2 + T_3}{2\Delta x} \tag{2}$$

where T_1, T_2, T_3 represent the temperatures measured from top to bottom by thermocouples located at the bottom of the microchannel near the outlet, Δx represents the vertical spacing between adjacent thermocouples, quantified as $\Delta x = 4$ mm.

The HTC at the outlet is calculated using Newton's law of cooling, where T_{w} is the wall temperature at the position of the downstream thermocouple, and T_{f} is the fluid temperature at the same location, obtained by linear interpolation of the inlet and outlet fluid temperatures:

$$h = \frac{q}{T_{\mathrm{w}} - T_{\mathrm{f}}} \tag{3}$$

The surface temperature at the microchannel outlet is determined through the application of the one-dimensional Fourier heat conduction equation:

$$T_{\mathrm{w}} = T_1 - q\left(\frac{x_1}{\lambda_{\mathrm{Cu}}}\right) \tag{4}$$

where $x_1 = 3.7$ mm denotes the microchannel's bottom wall's distance from the topmost thermocouple.

The difference between the measured inlet and outlet pressures of the microchannel test section is used to calculate the total flow boiling pressure drop:

$$\Delta P = P_{\mathrm{in}} - P_{\mathrm{out}} \tag{5}$$

where P_{in} and P_{out} denote the pressures at the inlet and outlet of the test section, respectively.

The uncertainty of the derived parameters is calculated using the uncertainty propagation formula proposed by Moffat [23]. The uncertainties of the relevant experimental parameters are listed in Table 1.

Table 1: Uncertainties of experimental parameters

Parameter	Uncertainty
H, W, L	±0.01 mm
M	±0.17%
T (K-type)	±0.50°C
T (T-type)	±0.20°C
P	±3.50%

(Continued)

Table 1 (continued)

Parameter	Uncertainty
q	±0.65%
T_w	±0.60%
h	±2.40%

4 Results and Discussions

4.1 Flow Patterns

Fig. 4 illustrates the flow pattern transition of HFE-7100 flow boiling in SSOMC at a mass flux of G = 1250.0 kg·m^{-2}·s^{-1}. As the heat flux escalated during the entire flow boiling process, the flow pattern sequentially evolved from bubbly flow (Fig. 4a) to a mixed bubbly-slug flow (Fig. 4b), and finally to churn flow (Fig. 4c). At low heat fluxes during the early stages of boiling, the flow pattern was dominated by bubbly flow. On the smooth surface, bubble nucleation required relatively high wall superheat, and the bubble growth rate on the SSOMC was relatively slow. Due to weak shear forces from the incoming flow, bubbles were not easily detached from the heat transfer surface. As the heat flux continued to increase, bubble growth became constrained by the channel width and the overlying open space, resulting in elongated, confined bubbles forming downstream along the flow direction. Meanwhile, the open space over the channel allowed the slug bubbles to exceed the channel height. Bubbly and slug bubbles coexisted along the channel, with slug bubbles predominantly concentrated downstream. Due to the limited number of nucleation sites on the SSOMC, the bubble size remained relatively small. At higher heat fluxes, vapor gradually occupied most of the flow passage, leading to more intense boiling and the formation of oscillatory churn flow, indicating that the SSOMC nearly approached the CHF condition.

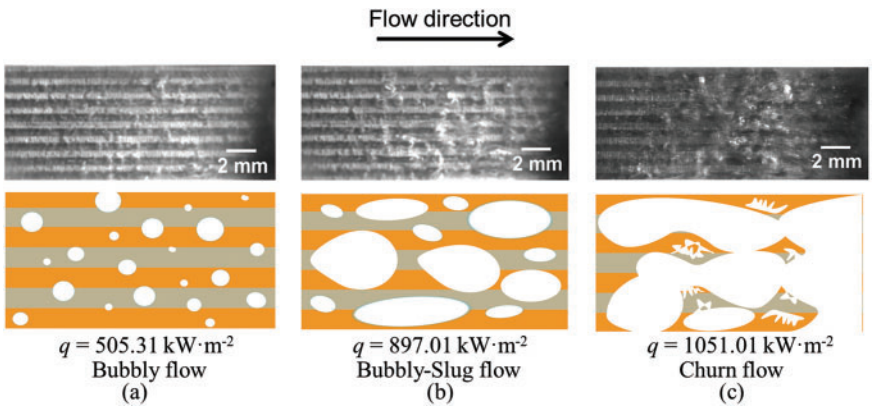

Figure 4: Flow patterns transition in SSOMC at G = 1250.0 kg·m^{-2}·s^{-1} and T_{in} = 30°C. (**a**) Bubbly flow; (**b**) Bubbly-slug flow; (**c**) Churn flow

Fig. 5 depicts the flow pattern transition of HFE-7100 flow boiling in MNSOMC at the same mass flux of G = 1250.0 kg·m^{-2}·s^{-1}. As heat flux increased, the flow pattern in MNSOMC evolved through four stages: bubbly flow (Fig. 5a), bubbly-slug flow (Fig. 5b), slug flow (Fig. 5c), and churn flow (Fig. 5d). The micro-nano composite structures, characterized by a microgrid array, enables early activation of nucleation sites at lower wall superheat, thereby reducing the superheat corresponding to the onset of nucleate boiling (ONB). The microgrid cavities and nanoscale particle structures significantly influenced bubble growth and

migration. The enhanced rewetting capability of the working fluid at the bottom surface enabled prompt liquid replenishment, while the resulting shear flow facilitated rapid bubble departure from the surface. Furthermore, due to the abundance of vaporization sites on the roughened surface of MNSOMC, adjacent low-surface-tension bubbles tended to quickly detach and merge in the axial direction, forming large bubbles with high aspect ratios, whose lengths along the flow direction were much greater than their widths perpendicular to the flow direction. As heat flux continued to rise, the bubble departure frequency increased and a large number of bubbles rapidly merged along the channel, expanding in both downstream as well as upstream directions. An annular liquid film developed between the continuous vapor slugs and the channel wall, marking the shift from bubbly flow to bubbly-slug flow. Upon the emergence of multiple elongated slug bubbles in the channel, the flow pattern shifted to slug flow. At high heat fluxes, continuous bubble expansion and intensified turbulence of the two-phase flow led to the development of churn flow. The degree of bubble agitation in MNSOMC was higher than in SSOMC, primarily attributable to the greater density of nucleation sites and higher bubble departure frequency facilitated via the micro-nano composite structures.

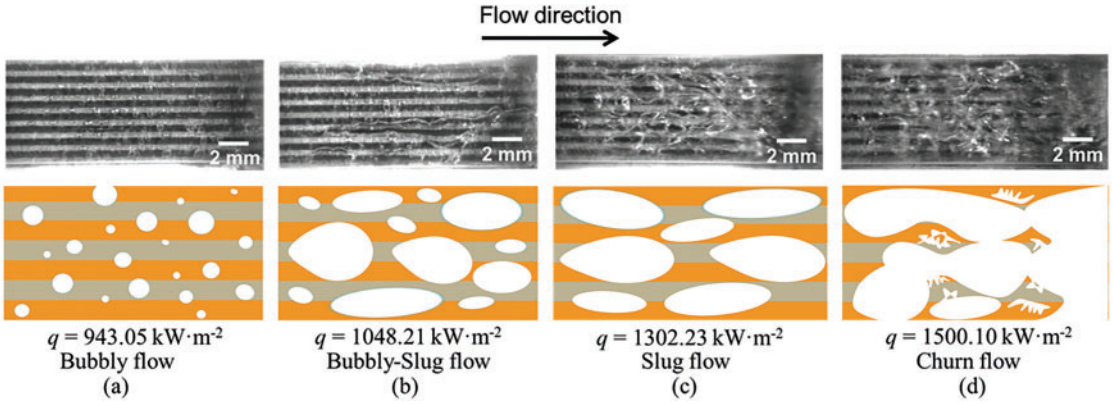

Figure 5: Flow patterns transition in MNSOMC at G = 1250.0 kg·m^{-2}·s^{-1} and T_{in} = 30°C. (**a**) Bubbly flow; (**b**) Bubbly-slug flow; (**c**) Slug flow; (**d**) Churn flow

4.2 Heat Transfer

Fig. 6a,b presents the boiling curves of HFE-7100 flow boiling in SSOMC and MNSOMC, respectively, under an inlet temperature of 30°C. Prior to the onset of boiling, the fluid in the microchannels remained in a single-phase convective heat transfer regime, during which the wall superheat increased significantly with rising heat flux. Subsequently, a sharp increase in the slope of the boiling curve marked the ONB. For MNSOMC, the ONB occurred earlier at all four mass fluxes, with a noticeable reduction in the corresponding wall superheat. Promoting the formation of more nucleation sites via hydrophilic surfaces can effectively enhance heat transfer performance [24]; the highly hydrophilic micro-nano composite structures of MNSOMC contained a large number of potentially active nucleation sites that were more easily activated, facilitating an earlier transition to two-phase heat transfer. After the ONB, the flow entered the two-phase regime, during which the working fluid removed a large amount of heat via latent heat of vaporization. The phase-change heat transfer was significantly enhanced compared to single-phase convective heat transfer. A local reduction in heat flux was observed in the boiling curve of MNSOMC, likely due to transient partial dryout or vapor film formation caused by high bubble coalescence rates. Similar phenomena have been reported in micro/nano structured boiling studies and reflect localized instability rather than global performance degradation. At moderate heat flux levels, boiling curves at different mass fluxes tended to

converge, indicating that mass flux had little influence on heat transfer during the nucleate boiling regime, where the dominant mechanism was nucleate boiling. With increasing mass flux, the two-phase convective heat transfer in MNSOMC was further enhanced, and the boiling curves exhibited an upward shift compared to SSOMC at the same mass flux. The high-aspect-ratio slug bubbles in MNSOMC retained larger continuous liquid films, which delayed the occurrence of local dryout. The efficient thin-film evaporation in the channels led to a higher CHF, with the HTC increasing by up to 33.4% and CHF by 33.1% at G = 1250.0 kg·m^{-2}·s^{-1}, reaching 1542.3 kW·m^{-2}.

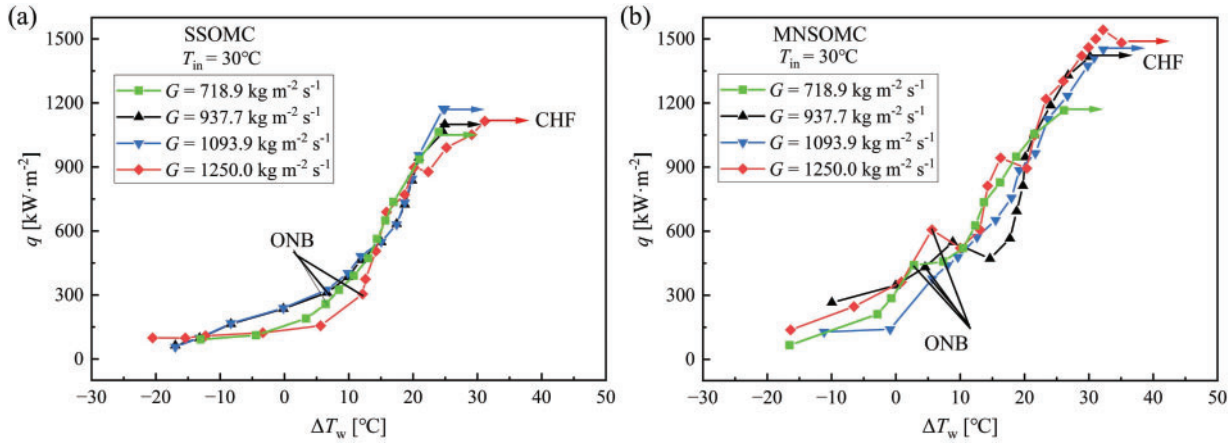

Figure 6: Flow boiling curves at inlet temperature T_{in} = 30°C in: (**a**) SSOMC. (**b**) MNSOMC

Fig. 7 shows the variation of HTC with heat flux and mass flux. It was observed that before boiling initiates, the HTC of both SSOMC and MNSOMC decreased to varying degrees as heat flux increased. This was attributed to the increase in specific heat at constant pressure and the decrease in thermal conductivity of single-phase HFE-7100 with temperature, leading to a net reduction in HTC. As heat flux continued to increase, nucleation sites on the wall became progressively activated, and the system transitioned into the flow boiling regime. The phase change of the working fluid absorbed a large amount of heat, and the intensifying nucleate boiling significantly increased HTC. In MNSOMC, the rapid coalescence of bubbles on the micro-nano structures and the vigorous vapor motion in the open space above the channels contributed to enhanced heat transfer under strong convective evaporation. At higher heat fluxes, the liquid replenishment to the heat transfer surface became insufficient to meet the vaporization demand at the liquid–vapor interface, and the HTC curve began to plateau, indicating an approach toward critical conditions. Near CHF, in SSOMC, bubble adhesion on the bottom heat transfer surface introduced thermal resistance that hindered further enhancement of heat transfer. In contrast, the superior wettability of MNSOMC led to better heat transfer performance. When liquid film evaporation occurred in the microchannel, the liquid transport on the micro-nano structured surface was more efficient, facilitating bubble departure by separating liquid and vapor paths, shortening the bubble residence time on the channel surface, and enabling rapid liquid replenishment to dried regions. This delayed the onset of CHF while increasing HTC, demonstrating that the micro-nano composite structures significantly enhanced the flow boiling heat transfer.

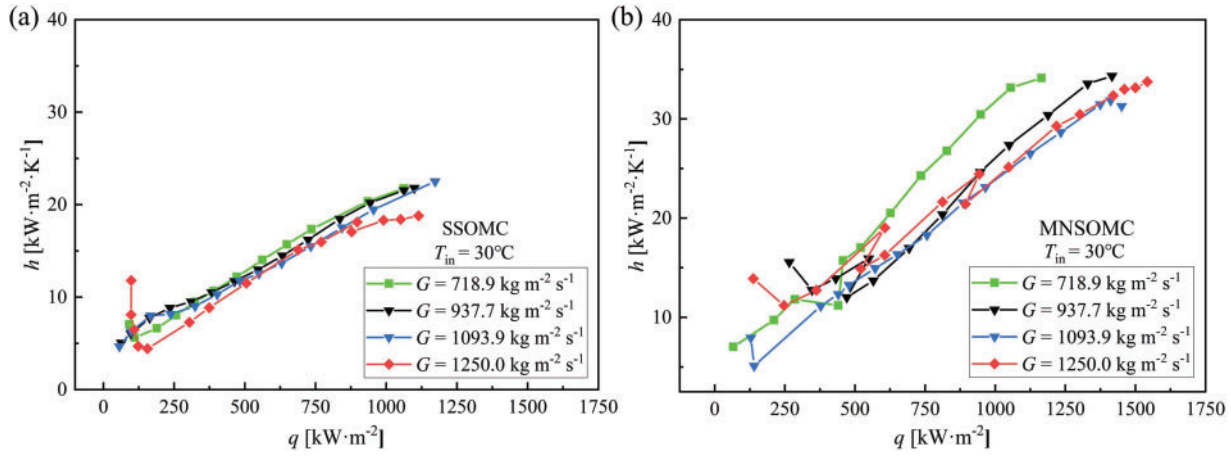

Figure 7: Flow boiling HTC at inlet temperature T_{in} = 30°C in: (**a**) SSOMC. (**b**) MNSOMC

4.3 Pressure Drop

Fig. 8 illustrates the variation of overall pressure drop with heat flux and mass flux in SSOMC and MNSOMC. Under single-phase flow conditions, the pressure drop in SSOMC exhibited a relatively low growth rate at low to moderate heat fluxes. Once boiling occurred within the channel, the flow pattern gradually shifted to bubbly flow and bubbly-slug flow. With increasing heat flux and mass flux, the number of bubbles and the vapor quality rose, resulting in continuous increases in both the frictional pressure drop and the vapor acceleration pressure drop of the two-phase flow. Under conditions of elevated heat fluxes, the two-phase flow within the channel entered a churn flow regime, during which the unstable and irregular vapor slugs in SSOMC intensified the turbulence and instability of the two-phase flow, resulting in substantial frictional pressure losses and a notable rise in the overall pressure drop. As shown in Fig. 8, in MNSOMC, the flow pattern transitioned toward slug flow and churn flow under moderate to large heat fluxes, but the pressure drop exhibited a more gradual increase with heat flux, and the variation across different mass fluxes remained relatively small. Compared to SSOMC, MNSOMC achieved enhanced heat transfer performance without incurring greater pressure drop. This was attributed to the micro-nano structures on the heat transfer surface of MNSOMC, which enhanced the surface's wettability and facilitate the formation of a stable liquid film on the heat sink surface. The resulting lubrication effect reduced the near-wall shear stress and frictional pressure drop. Furthermore, the liquid–vapor path separation provided by the highly hydrophilic micro-nano composite structures of MNSOMC helped attenuate turbulence within the two-phase flow over a wider range of heat fluxes, thereby continuously lowering the corresponding pressure drop. Consequently, MNSOMC exhibited lower two-phase pressure drops than SSOMC, along with a slower rate of pressure drop increase.

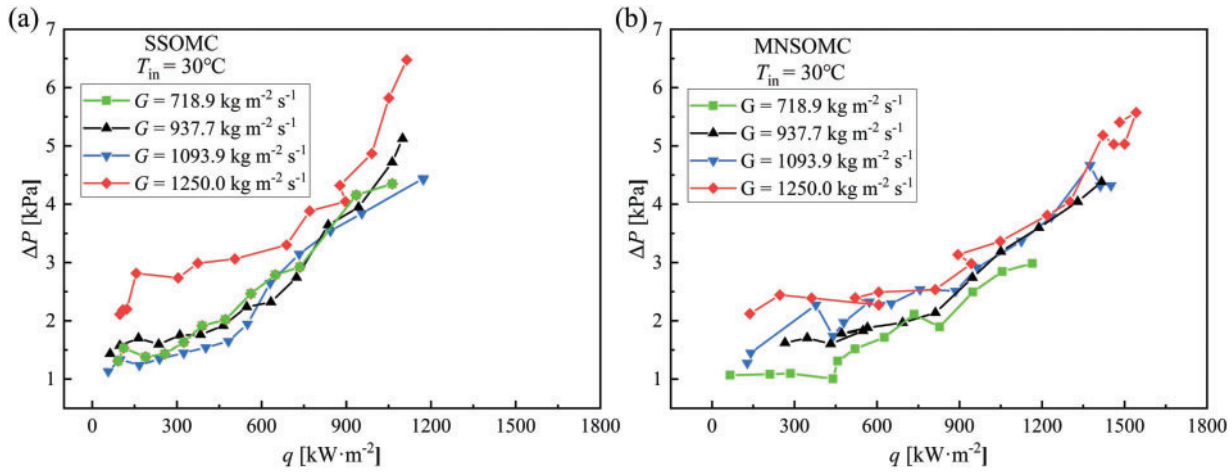

Figure 8: Flow boiling HTC at inlet temperature T_{in} = 30°C in: (**a**) SSOMC. (**b**) MNSOMC

5 Conclusions

In this study, micro-nano composite structures were fabricated on the bottom surface of open microchannels using laser ablation technology. A high-speed camera was employed to examine the bubble dynamics and flow pattern evolves during the subcooled flow boiling of HFE-7100 in both smooth-surface open microchannels (SSOMC) and open microchannels with micro-nano composite structures (MNSOMC). A comparative investigation was conducted on the flow boiling characteristics in the two test sections. The primary conclusions are outlined below:

(1) With increasing heat flux, three distinct flow patterns—bubbly flow, bubbly-slug flow, and churn flow-were successively observed in the SSOMC. In the MNSOMC, the flow initially appeared as bubbly flow with relatively large bubble sizes. At moderate heat fluxes, the dominant flow patterns were bubbly-slug and slug flow, with a large number of elongated slug bubbles present in the channel. At higher heat fluxes, the flow transitioned into churn flow, and the intensity of bubble agitation increased markedly as the system gradually approached critical conditions.

(2) The laser-ablated micro-nano composite structures significantly enhanced the CHF and HTC of HFE-7100 flow boiling in open microchannels. Under the experimental conditions of this study, the HTC in the MNSOMC maximally increased by 33.4% and the CHF maximally improved by 133.1% compared to the SSOMC, reaching 1542.3 kW·m^{-2}. The abundant nucleation sites and strong surface wettability of the MNSOMC promoted rewetting of the bubble nucleation sites by the liquid and facilitated rapid bubble departure. Moreover, the large number of bubbles generated on the channel wall tended to coalesce longitudinally to form high aspect ratio slug bubbles, which enhanced thin film evaporation and thus improved the boiling heat transfer performance.

(3) While enhancing the flow boiling heat transfer, the MNSOMC maintained a two-phase pressure drop comparable to or even slightly lower than that of the SSOMC. The lubrication effect induced by rapid bubble departure and the high surface wettability reduced the frictional pressure drop, while the presence of stable, regularly shaped high aspect ratio bubbles suppressed two-phase turbulence, thereby mitigating the pressure drop penalty.

This study provides an initial comparison between a smooth surface and a laser-textured micro-nano composite surface in open microchannels. However, the enhancement mechanism of micro-nano structures is highly dependent on geometrical features such as cavity size, aspect ratio, and spacing.

Future work will involve a systematic investigation of different micro/nano topographies to quantitatively evaluate their individual and synergistic effects on bubble dynamics, flow pattern transitions, and heat transfer performance.

Acknowledgement: Not applicable.

Funding Statement: This research was funded by the National Natural Science Foundation of China (Grant No. 52276047), the Open Fund of National Key Laboratory of Spacecraft Thermal Control (Grant No. NKLST-JJ-202401011), and the Beijing Municipal Science & Technology Commission (Grant No. Z231100006123010).

Author Contributions: Conceptualization, Liaofei Yin; validation, Kexin Zhang, Wenhao Ma; investigation, Liaofei Yin, Kexin Zhang; data curation, Kexin Zhang, Tianjun Qin; writing—original draft preparation, Liaofei Yin, Kexin Zhang; writing—review and editing, Liaofei Yin, Kexin Zhang; visualization, Yi Ding; supervision, Liaofei Yin; project administration, Yawei Xu; funding acquisition, Liaofei Yin. All authors reviewed the results and approved the final version of the manuscript.

Availability of Data and Materials: Data are contained within the article.

Ethics Approval: Not applicable.

Conflicts of Interest: The authors declare no conflicts of interest to report regarding the present study.

Nomenclature

Symbols

G	Mass flux, $kg \cdot m^{-2} \cdot s^{-1}$
H	Height, m
h	Heat transfer coefficient, $kW \cdot m^{-2} \cdot K^{-1}$
L	Length, m
P_{in}	Inlet pressure, Pa
P_{out}	Outlet pressure, Pa
ΔP	Total pressure drops, Pa
q	Heat flux, $kW \cdot m^{-2}$
T	Temperature, °C
T_f	Fluid temperature, °C
T_{out}	Outlet temperature, °C
T_w	Wall temperature, °C
T_{sat}	Saturation temperature, °C
W	Width, m
x_1	Distance, m

Greek Symbols

λ_{Cu}	Thermal conductivity of copper, $W \cdot m^{-1} \cdot K^{-1}$

Abbreviations

CHF	Critical heat flux
HTC	Heat transfer coefficient
MNSOMC	Micro-nano structured open microchannels
ONB	Onset of nucleate boiling
SEM	Scanning electron microscope
SSOMC	Smooth-surface open microchannels

References

1. Garimella SV, Persoons T, Weibel JA, Gektin V. Electronics thermal management in information and communications technologies: challenges and future directions. IEEE Trans Compon Packag Manuf Technol. 2017;7(8):1191–205. doi:10.1109/tcpmt.2016.2603600.
2. Mao N, Zhuang J, He T, Song M. A critical review on measures to suppress flow boiling instabilities in microchannels. Heat Mass Transf. 2021;57(6):889–910. doi:10.1007/s00231-020-03009-2.
3. Fang Y, Lu D, Yang W, Yang H, Huang Y. Saturated flow boiling heat transfer of R1233zd(E) in parallel minichannels: experimental study and flow-pattern-based prediction. Int J Heat Mass Transf. 2023;216(1):124608. doi:10.1016/j.ijheatmasstransfer.2023.124608.
4. Costa-Patry E, Olivier J, Thome J. Heat transfer charcacteristics in a copper micro-evaporator and flow pattern-based prediction method for flow boiling in microchannels. Front Heat Mass Transf. 2012;3(1):1–14. doi:10.5098/hmt.v3.1.3002.
5. Fattahi R, Saidi M. Numerical investigation of curved shape fins height effect on heat transfer and flow characteristics in open microchannel heat sink. Int J Therm Sci. 2023;185(3):108060. doi:10.1016/j.ijthermalsci.2022.108060.
6. Zhao Q, Zhang D, Qiu J, Lu M, Zhou J, Chen X. Bubble behaviors and flow boiling characteristics in open microchannels with large aspect ratio. Appl Therm Eng. 2022;213:118768. doi:10.1016/j.applthermaleng.2022.118768.
7. Bhandari P, Prajapati YK. Thermal performance of open microchannel heat sink with variable pin fin height. Int J Therm Sci. 2021;159(2):106609. doi:10.1016/j.ijthermalsci.2020.106609.
8. Bhandari P, Prajapati YK. Influences of tip clearance on flow and heat transfer characterstics of open type micro pin fin heat sink. Int J Therm Sci. 2022;179(11):107714. doi:10.1016/j.ijthermalsci.2022.107714.
9. Cao S, Yang H, Zhao L, Wang T, Xie J. Recent advances of surface wettability effect on flow boiling heat transfer performance. Front Heat Mass Transf. 2021;17:1–16. doi:10.5098/hmt.17.17.
10. Sathyanarayana A, Warrier P, Joshi Y, Teja A. Saturated and subcooled pool boiling of HFE-7200 mixtures on a copper nanowire surface. Front Heat Mass Transf. 2012;2(4):1–7. doi:10.5098/hmt.v2.4.3007.
11. Chang W, Luo K, Li W, Li C. Enhanced flow boiling of HFE-7100 in silicon microchannels with nanowires coated micro-pinfins. Appl Therm Eng. 2022;216:119064. doi:10.1016/j.applthermaleng.2022.119064.
12. Zhuang X, Xie Y, Li X, Yue S, Wang H, Wang H, et al. Experimental investigation on flow boiling of HFE-7100 in a microchannel with pin fin array. Appl Therm Eng. 2023;225(7):120180. doi:10.1016/j.applthermaleng.2023.120180.
13. Li W, Li C, Wang Z, Chen Y. Enhanced flow boiling in microchannels integrated with supercapillary pinfin fences. Int J Heat Mass Transf. 2022;183(4):122185. doi:10.1016/j.ijheatmasstransfer.2021.122185.
14. Yang F, Li W, Dai X, Li C. Flow boiling heat transfer of HFE-7000 in nanowire-coated microchannels. Appl Therm Eng. 2016;93:260–8. doi:10.1016/j.applthermaleng.2015.09.097.
15. Alam T, Li W, Chang W, Yang F, Khan J, Li C. Favourably regulating two-phase flow regime of flow boiling HFE-7100 in microchannels using silicon nanowires. Sci Rep. 2021;11(1):11131. doi:10.1038/s41598-021-89466-z.
16. Zhou L, Li W, Ma T, Du X. Experimental study on boiling heat transfer of a self-rewetting fluid on copper foams with pore-density gradient structures. Int J Heat Mass Transf. 2018;124(3):210–9. doi:10.1016/j.ijheatmasstransfer.2018.03.070.
17. Khan SA, Sezer N, Koç M. Design, fabrication and nucleate pool-boiling heat transfer performance of hybrid micro-nano scale 2-D modulated porous surfaces. Appl Therm Eng. 2019;153(11):168–80. doi:10.1016/j.applthermaleng.2019.02.133.
18. Liu B, Yu L, Zhang Y, Marco PD, Wei J. Enhanced nucleate pool boiling by coupling the pinning act and cluster bubble nucleation of micro-nano composited surfaces. Int J Heat Mass Transf. 2020;157(11):119979. doi:10.1016/j.ijheatmasstransfer.2020.119979.
19. Shin S, Choi G, Kim BS, Cho HH. Flow boiling heat transfer on nanowire-coated surfaces with highly wetting liquid. Energy. 2014;76(1):428–35. doi:10.1016/j.energy.2014.08.037.
20. Može M, Zupančič M, Hočevar M, Golobič I, Gregorčič P. Surface chemistry and morphology transition induced by critical heat flux incipience on laser-textured copper surfaces. Appl Surf Sci. 2019;490:220–30. doi:10.1016/j.apsusc.2019.06.068.

21. Doran B, Zhang B, Walker A, Kc P, Meng WJ, Moore AL. Experimental determination of the role of increased surface area in pool boiling from nanostructured surfaces. Exp Therm Fluid Sci. 2020;111:109956. doi:10.1016/j.expthermflusci.2019.109956.
22. Zhang S, Chen G, Jiang X, Li Y, Shah SWA, Tang Y, et al. Hierarchical gradient mesh surfaces for superior boiling heat transfer. Appl Therm Eng. 2023;219:119513. doi:10.1016/j.applthermaleng.2022.119513.
23. Moffat RJ. Describing the uncertainties in experimental results. Exp Therm Fluid Sci. 1988;1(1):3–17. doi:10.1016/0894-1777(88)90043-X.
24. Chen J, Ahmad S, Deng W, Cai J, Zhao J. Micro/nanoscale surface on enhancing the microchannel flow boiling performance: a Lattice Boltzmann simulation. Appl Therm Eng. 2022;205:118036. doi:10.1016/j.applthermaleng.2022.118036.